Gust mitigation through closed-loop control. II. Feedforward and feedback control

Benjamin Herrmann, Steven L. Brunton, Johannes E. Pohl, and Richard Semaan

Phys. Rev. Fluids **7**, 024706 — Published 10 February 2022

DOI: 10.1103/PhysRevFluids.7.024706

Gust mitigation through closed-loop control. Part II: feedforward and feedback control

Benjamin Herrmann*
Department of Mechanical Engineering, Universidad de Chile, Beauchef 851, Santiago, Chile

Steven L. Brunton
Department of Mechanical Engineering, University of Washington, Seattle, WA 98195, USA

Johannes E. Pohl and Richard Semaan†
Institute of Fluid Mechanics, Technische Universitt Braunschweig, Braunschweig, 38106, Germany
(Dated: January 6, 2022)

Wing-gust encounters arising from flight over complex terrain or adverse weather are unavoidable and cause large lift transients that may result in structural damage due to extreme loads and or fatigue. Gust mitigation through control has the potential to extend the lifetime of air vehicles and wind turbines, although it is challenged by sensor noise, time-delays, and low latency requirements. In this study, we report on the successful design and deployment of a closed-loop controller to regulate the lift coefficient of an airfoil equipped with an actuated trailing-edge flap against vortical gust disturbances. The approach is served by a feedforward-feedback control strategy and dedicated hardware. The control strategy relies on the characterization and modeling of the lift response to flap deflections and gust disturbances. In Part I of this series, we quantify and model the lift response to flap deflections. In this second part, we examine and model the gust disturbances on the airfoil lift and combine the models within the control architecture. Gust characterization reveals previously unknown synergy between concurrent gusts with opposite rotation direction, yielding large bursts of lift. The lift response model to gust disturbances is compared to Küssner's and validated against experimental results. The model-based feedforward loop detects the onset and magnitude of gust disturbances, which are generated upstream by a pitching airfoil, through a two-component X-wire located upstream of the DLR-F15 research airfoil. The combined controller proves to be effective for lift regulation during gust encounters, with feedforward rejecting large disturbances, and feedback attenuating high-frequency sensor noise and compensating for model uncertainty.

I. INTRODUCTION

Passenger aircraft, wind turbines, and micro-air vehicles experience unsteady forces and moments when crosswind and or longitudinal velocity disturbances (gusts) occur relative to their direction of motion. The unsteady loads produced by gusts can be strong enough to cause structural damage and may also result in loss of control of the aerodynamic surfaces. Due to its potential to extend the lifetime and reliability of these systems, gust mitigation through control has recently been investigated using a variety of strategies such as blown jets [1], synthetic jets [2], and control surfaces [3], among others. In this work, we employ a trailing edge flap for active control with the objective of regulating airfoil lift when encountering gust disturbances.

Gust disturbances refer to coherent perturbations of a uniform free-stream flow encountered by an immersed body. These may take many forms and are often classified into three canonical cases: transverse, vortical, and streamwise gusts [4]. Accurate models of the unsteady aerodynamic response of an airfoil during a gust encounter are critical for control applications due to sensor noise, time delays, and short response-time requirements. There are several models based on potential flow theory that build on Wagner's indicial response [5] and Theodorsen's frequency response [6]. The case of an airfoil entering a sharp-edged transverse gust region was addressed by Küssner [7] and later by von Kármán and Sears [8]. The response to a harmonically oscillating gust field was studied by Sears [9] for the transverse case and by Greenberg [10] for the streamwise case. Although all of these models are convenient and easy to implement, they rest on assumptions that are often not valid in applications of interest, namely infinitesimal disturbances, a zero-thickness airfoil, attached flow, and a planar and rigid wake [11].

During the last decade, these practical challenges have motivated numerous experimental studies to characterize gust disturbances and the airfoil lift response they induce [4]. Various investigations have focused on harmonically oscillating streamwise gusts [12, 13], sine-squared transverse gusts [14, 15], travelling transverse gusts [16], top-hat

* benjaminh@uchile.cl
† r.semaan@tu-bs.de

shaped transverse gusts [17], and vortical gusts [18–20]. Except for the work by Klein et al. [18], all of these studies have considered low Reynolds numbers, on the order of $Re = 5 \cdot 10^4$ or lower, which is representative of the fluid dynamics for micro-air vehicles but not aircraft. For transverse gusts at these low Re, Küssner's model along with Duhamel's superposition integral was found to perform well at predicting the lift response [14, 15, 17], even though many of the theoretical assumptions are not respected. Whether or not this good predictive performance holds for higher Reynolds numbers is yet to be investigated.

Away from the idealized conditions of thin-airfoil theory, numerical simulations have been successful at characterizing unsteady aerodynamics at low Reynolds numbers [21–25]. Low-order models of the unsteady loads, suitable for flow control applications, have been obtained or tuned using data [2, 26–31]. Kerstens et al. [26] used wind tunnel measurements to identify unsteady lift models for an airfoil in response to pulsed-blowing actuation and to the wind tunnel speed during streamwise gusts. Both, actuation and disturbance response models were used to design a robust H_∞ closed-loop controller that successfully regulated lift by incorporating feedforward control that used hot-wire measurements of the free-stream velocity fluctuations. Williams and King [2] discussed the practical benefits and limitations of gust mitigation using active flow control. Recently, Sedky et al. [31] investigated the control of a sine-squared transverse gust in water tank experiments at $Re = 40000$. Their control architecture was based on an experimentally calibrated Goman-Khrabrov model and considered an unscented Kalman filter for state estimation followed by full-state feedback with hand-tuned gains. The authors used the control signal generated from closed-loop control simulations in response to a known gust disturbance to perform open-loop control experiments, resulting in up to 50% mitigation of the peak lift fluctuation.

In this work, we regulate airfoil lift during vortical gust encounters at aircraft-relevant Reynolds number $Re = 1.8 \cdot 10^6$ using an active trailing edge flap. This is achieved by combining feedback control that is based on time-resolved lift measurements, and feedforward control that relies on two-component flow velocity readings from an X-wire sensor located upstream of the airfoil. In the first article of this two-part series, we characterize and model the lift response to flap pitching. In this second paper, we quantify and model the lift response to gust disturbances, and present our control strategy and report on its performance in mitigating gust effects.

II. EXPERIMENTAL SETUP

A. Wind tunnel setup

The experiment is conducted in the Modell-Unterschallkanal Braunschweig (MUB) wind tunnel at the Institute of Fluid Mechanics of the Technische Universitt Braunschweig. The MUB is a low-speed closed circuit wind tunnel with a test section of $1.3\,\mathrm{m} \times 1.3\,\mathrm{m} \times 5.7\,\mathrm{m}$. Flow speeds of up to $60\,\mathrm{m/s}$ can be achieved in the test section. In the current experiment, the incident flow is maintained at a constant velocity of $U_\infty = 50\,\mathrm{m/s}$ and a constant temperature of $\approx 36\,^\circ\mathrm{C}$.

The experimental setup in the wind tunnel test section is presented in Fig. 1, showing the gust generator in the near field and the research airfoil in the back. The experimental setup from a side view and relevant parameters, such as the gust generator angle of attack α_G, the airfoil angle of attack α, and its flap angle δ are shown in Fig. 2. Also illustrated are two X-wire positions XW1 ($x/c = -2.53$) and XW2 ($x/c = -1.16$), where the two velocity components along x and z are measured. The research airfoil is a DLR-F15 airfoil with a chord length of $c = 600\,\mathrm{mm}$, resulting in a chord Reynolds number $Re \approx 1.8 \cdot 10^6$. It is equipped with a trailing edge flap adapted from the clean airfoil configuration with a chord length of $c_\mathrm{F} = 0.1 \cdot c = 60\,\mathrm{mm}$. A gap of approximately 1 mm is present between the main airfoil trailing edge and the flap leading edge to allow free rotation. No sealing is applied across the gap. Two ESR Pollmeier MH4251 servo motors with a nominal torque of $14\,\mathrm{N\,m}$ each and an electric time constant $\tau_\mathrm{el} = 1.12\,\mathrm{ms}$ are used to deflect the flap by up to $\delta = \pm 25\,^\circ$.

The gust generation system consists of a NACA-0021 airfoil with a chord length of $c_\mathrm{G} = 300\,\mathrm{mm}$, that is actuated by two Copley XTA 3806 linear servo motors on each side [18]. The four actuators are synchronized by a master-slave control system. Multiple mechanical and digital safety measures are employed to ensure synchronization and to avoid excessive mechanical loads. The four servo motors yield deflection rates of up to $20\,^\circ$ in 20 ms, leading to the formation of start-stop vortices that convect downstream to simulate vortex gust encounters. The rotation axes denoted by the black dot in Fig. 2 is located 120 mm ($x/c_\mathrm{G} = 0.4$) from the leading edge. The gust generator trailing edge is situated $x/c = -3.49$ (2091 mm) upstream of the research airfoil, allowing enough time for the gusts to develop. The spanwise uniformity of the generated vortex gusts was verified in a previous study by spanwise measurements upstream of the DLR-15 airfoil that showed a deviation of less than 3.5% in velocity magnitude [18]. The entire setup including the gust generator and the servo controllers is commanded by the main data acquisition and control system, a NI cRIO-9039 FPGA controller.

FIG. 1. Experimental setup inside the MUB test section showing the NACA-0021 gust generator airfoil (front), the hot wire probe, and the DLR-F15 research airfoil (back).

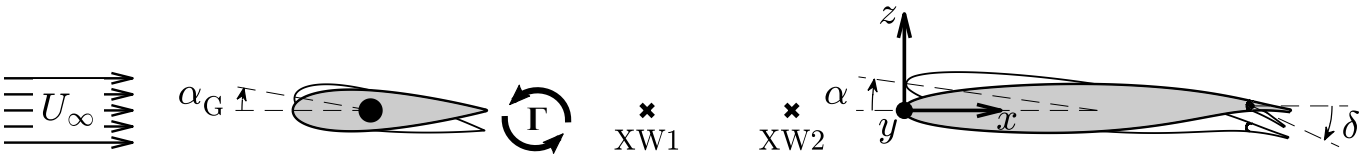

FIG. 2. Schematics of wind tunnel setup including the gust generator, the two X-wire positions XW1 ($x/c = -2.53$) and XW2 ($x/c = 1.16$), and the DLR-F15 research airfoil. Also shown are the gust generator angle of attack α_G, the airfoil angle of attack α, and the flap angle δ. Not all dimensions are to scale.

B. Acquisition and control systems

In this second part of the series, we mainly report on our gust characterization and mitigation efforts. Critical to these efforts is the real-time acquisition of the flow velocity upstream of the airfoil to detect the gust onset and its characteristics. This is achieved using a constant temperature anemometry (CTA) X-wire system connected to a Dantec Streamline Pro anemometer that measures the x and z flow velocity components. Two locations denoted by XW1 ($x/c = -2.53$, $y/c = -0.83$, $z/c = 0$) and XW2 ($x/c = 1.16$, $y/c = -0.83$, $z/c = 0$) are individually tested. The position in the z direction is the least biased location at the mid-height of the test section, and aligns with the two airfoil chordlines. The 150 mm ($y/c = -0.83$) distance to the side wall is selected after multiple tests in the spanwise direction to ensure gust disturbances are measured outside the side wall boundary layer, while minimizing the probe holder wake effects on the airfoil. Hot-wires provide the most accurate and time-resolved point measurements in a controlled wind tunnel environment. However, their fragility limits their deployment on aircraft. Instead, aircraft may use, for example, multi-hole pressure probes or LIDAR (Light Detection and Ranging) systems. LIDAR system employment for disturbance detection is a current active field of research.

Similarly critical to our objectives is the instantaneous acquisition of the lift coefficient, which we achieve using a mapping technique [32] based on 16 time-resolved and 84 steady pressure sensors located along the airfoil midspan (c.f. Fig. II B). This mapping is necessary to correct for the relatively coarse pressure distribution obtained from the time-resolved pressure sensors (red dots in Fig. II B). The mapping relies on piecewise correction of the unsteady surface pressure to the closest steady curve segment from a large library of distributions. The steady pressure taps with 0.3 mm diameter are connected to a DTC Initium system with calibrated ESP-HD type pressure scanners with $\pm 0.05\,\%$ full-scale accuracy. The Honeywell SDX05D4 fast pressure sensors acquire the surface pressure through 50 – 150 mm long and 0.8 mm diameter tubes. In-situ step response tests of the Honeywell sensors have shown negligible time delay and signal distortion in the frequency range of interest. The transducers feature passive temperature compensation, and a live offset adjustment ensures matching pressures between the time-resolved and the steady pressure sensors.

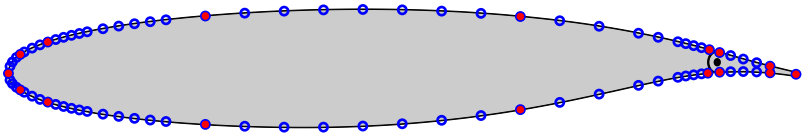

FIG. 3. Pressure sensor distribution over the DLR-F15 airfoil midspan. Blue circles indicate steady pressure taps, whereas red dots represent time-resolved pressure measurement locations.

The third type of measured data is the flap angular position, which is acquired by two Sick DFS60 differential position encoders with a 20" resolution installed on the two flap driveshafts so that the flap position can be acquired directly without the need to account for twist in the safety clutches.

All acquisition and control processes are centrally managed by a LabVIEW code running on the FPGA of the cRIO-9039 at a rate of 100 kHz, which ensures that all data and tasks are processed in real-time. The code handles all data acquisition, initial processing, and control tasks autonomously on the FPGA. The live sampled data is transmitted to a host PC for monitoring and recording.

C. Test cases

The presented results are the outcome of three measurement campaigns that sequentially constructed the necessary components for model-based closed-loop gust control. In the first campaign, whose results are detailed in Part I of the series, the flow response to the harmonically pitching flap was characterized and modeled. In the second and third campaigns, which provide the bulk results of the current manuscript, we report on the gust characterization and modeling efforts and the closed-loop control strategy used to mitigate gust effects on the lift.

The gust generator described in section II A is capable of producing a range of vortical gusts, whose characteristics depend on the angle of attack change $\Delta\alpha_\mathrm{G}$ and the pitch rate $\dot{\alpha}_\mathrm{G}$. Two pitch rates $\dot{\alpha}_\mathrm{G} = 200\,^\circ/\mathrm{s}$ and $\dot{\alpha}_\mathrm{G} = 1000\,^\circ/\mathrm{s}$ are tested for a range of pitch amplitudes $\Delta\alpha_\mathrm{G}$, with $\alpha_\mathrm{G} \in [-12\,^\circ,\ 12\,^\circ]$. This corresponds to non-dimensional pitch rates of $\dot{\alpha}^*_\mathrm{G} = 0.042$ and $\dot{\alpha}^*_\mathrm{G} = 0.209$, where $\dot{\alpha}^*_\mathrm{G} = \dot{\alpha}_\mathrm{G} \cdot c/U_\infty$ is in units radians per convective time. These diverse pitching conditions yield a range of gust ratios $0 < \mathrm{GR} < 0.1$ and gust encounter widths $0 < W < 3$, where

$$\mathrm{GR} = \frac{V}{U_\infty}\,,$$

and

$$W = \frac{w}{c}\,,$$

where V is the magnitude of the flow velocity disturbance, and w is the gust width measured from its center [4]. Two pitching motions are investigated: *periodic* with a constant pause between pitches ($\alpha_{\mathrm{G}0} = -12\,^\circ$, $\alpha_{\mathrm{G}1} = 12\,^\circ$, $\Delta t^* = 2tU_\infty/c \approx 42$), and *quasi-random* with varying pitch amplitude and hold time ($\alpha_{\mathrm{G}0}$, $\alpha_{\mathrm{G}1} \in [-12\,^\circ,\ 12\,^\circ]$, $\Delta t^* \in [0,\ 42]$). The quasi-random maneuvers considered are pitch-stop motions, where the pitching amplitude and the duration of the pauses are randomly sampled from a triangular distribution. The probability density functions of both, the target (dashed) and the resulting measured (solid blue) pitch amplitude are shown in Fig. 4. As the figure shows, the resultant pitch amplitudes follow the theoretical distribution, except at around $\Delta\alpha_\mathrm{G} = 0$, which corresponds to no pitching. Hence, the gap in the middle is caused by samples that are too small to register as a pitch maneuver. Whereas the periodic motion offers regular and interpretable gusts, the quasi-random motion yields more realistic scenarios that are more challenging for closed-loop control. All experiments are conducted at 3 angles of attack, $\alpha = 0, 5, 8\,^\circ$.

III. CONTROL STRATEGY AND LIFT RESPONSE MODELING

The main contribution of this manuscript is the development and deployment of a model-based closed-loop control strategy to mitigate gust disturbances. The strategy, illustrated in Fig. 5, consists of a feedback and feedforward loop. The control objective is to track a reference lift coefficient r while rejecting large disturbances and attenuating high-frequency sensor noise. The control strategy requires the development of multiple models.

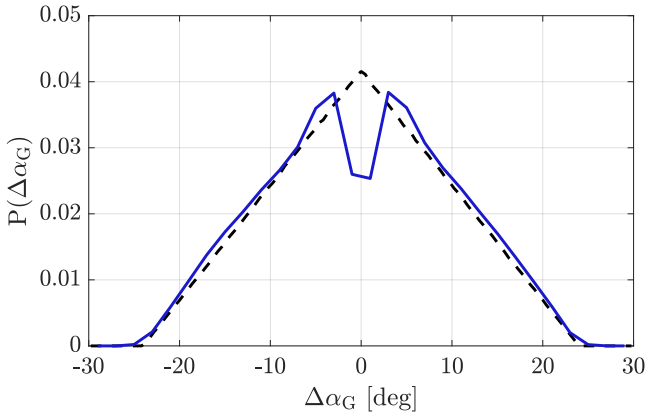

FIG. 4. Probability density function distributions of the theoretical (dashed) and measured (solid blue) gust generator pitch amplitude $\Delta\alpha_G$ for the quasi-random actuation motion.

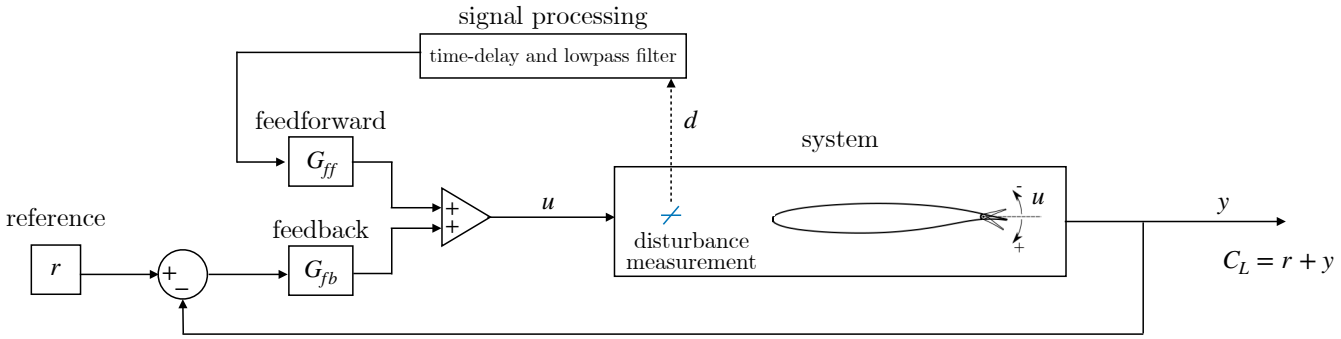

FIG. 5. Block diagram for the implemented control setup.

The lift model combines two response models to flap actuation G_{yu} and to gust disturbances G_{yd}, to yield a model structure in the frequency domain as

$$y = G_{yu}u + G_{yd}d, \tag{1}$$

where, following the notation from control theory, $y = C_L - r$ is the deviation of the lift coefficient from a reference value r, $u = \delta$ is the control input that is the flap deflection angle, and $d = [U - U_\infty \; V]^T$ are the external disturbances relayed by the X-wire velocity measurements. The models G_{yu} and G_{yd} are identified from experimental data, as detailed in the following subsections. As shown in Fig. 5, the filtered and time-shifted signal d is then fed to a feedforward controller G_{ff} as

$$G_{ff} = -G_{yu}^{-1}G_{yd}\,. \tag{2}$$

This transfer function takes as an input the real-time disturbance measurements d and outputs the control signal u necessary to counteract the gust effects using the active trailing edge flap.

In addition, the control strategy also includes a feedback controller G_{fb}, as shown in Fig. 5. This transfer function maps the deviation between the reference and the measured lift coefficient y to a correction in the flap deflection angle u to provide reference tracking and compensate for model uncertainty in the feedforward controller while attenuating sensor noise. We investigate two different feedback controllers, one model-based and one model-free architecture. For the model-based controller, an H_∞ loop-shaping [33] design is considered, where the closed-loop transfer function is chosen to be an integrator (s^{-1}) with a crossover frequency $f_c = 5\,\mathrm{Hz}$, to provide reference tracking for frequencies below f_c and noise attenuation for frequencies higher than f_c. This translates into a control transfer function

$$G_{fb} = \frac{2\pi f_c}{s}G_{yu}^{-1}\,. \tag{3}$$

For the model-free feedback, a PI (proportional-integral) controller is considered with a transfer function of the form

$$G_{fb} = \frac{K_p s + K_i}{s}, \tag{4}$$

TABLE I. Identified transfer function coefficients for the lift response to flap actuation G_{yu} at various airfoil angles of attack α.

α	a_0	a_1	a_2	b_0	b_1	b_2
0 deg	1.93485	5.13803	1.41021	1.107	5.793	1.000
5 deg	3.29235	7.65731	1.59824	2.029	8.652	1.000
8 deg	0.53078	1.34597	1.00432	0.369	1.451	1.000

where the proportional and integral coefficients $K_p = 0.25\,\mathrm{V}/^\circ$ and $K_i = 0.02\,\mathrm{V}/^\circ\mathrm{s}$ are experimentally calibrated. We note that, unlike the model-based feedback control, the PI controller is constructed to yield a direct voltage signal to the servo motors driving the flap.

In the remainder of this section, we detail the two lift response models, which constitute the main components of our control strategy.

A. Lift response model to flap actuation

The current setup relies on the trailing-edge flap actuation to counteract disturbances generated by wing-gust encounters. Given the characteristics of the generated gust disturbances, presented in section IV A, actuation using small flap deflection angles and moderate reduced frequencies is deemed sufficient to fulfill our set control objectives. Conveniently, over that range of inputs, the frequency response of the unsteady lift under harmonic flap pitching behaves linearly. Therefore, linear lift response models are built for $\alpha = 0^\circ,\ 5^\circ$ and 8°, a mean pitch angle $\delta_0 = 0^\circ$, pitching amplitudes $\delta_1 < 10^\circ$, and reduced frequencies $k = \omega\, c/2\, U_\infty < 0.75$, as detailed in Part I of this series.

The models are transfer functions with two poles and two zeros, with the flap deflection angle as the input and the unsteady lift coefficient as the output. Hence, the models have the following structure

$$G_{yu}(s) = \frac{a_2 s^2 + a_1 s + a_0}{b_2 s^2 + b_1 s + b_0}, \tag{5}$$

where $s = fc/(2U_\infty)$ is in reduced frequency units, with f being the frequency in Hz. For completeness, the model coefficients identified in part I of this series are repeated in Tab. I for the three airfoil angles of attack.

A comprehensive assessment of the lift response model to flap actuation is provided in Part I of this series, where a comparison to thin airfoil theory approximations and to the experimental results is reported.

B. Lift response model to gust disturbances

We now turn our attention to modeling the unsteady lift generated during gust encounters. Specifically, we are interested in a linear model that receives the two velocity components measured by the X-wire sensor and outputs the lift coefficient. The models are trained and tested on two distinct quasi-random gust maneuvers, where the instantaneous time-series of the X-wire signals and the lift coefficient are used as input and output signals, respectively. The two quasi-random realizations are faithfully replicated ten times for better statistical averaging [34]. These experiments are additionally repeated for the two X-wire positions XW1 and XW2 upstream of the DLR-F15 airfoil leading edge for flap deflection angles of $\delta = -5^\circ,\ 0^\circ$, and 5°, and angles of attack of $\alpha = 0^\circ,\ 5^\circ$, and 8°.

For all combinations of gust generator maneuvers, X-wire positions, flap deflection angles, and airfoil angles of attack, the data are processed as follows. First, recordings obtained from repeated maneuvers are time-aligned based on the X-correlation between lift coefficient signals. Alignment is necessary to account for the dead-time τ between the gust disturbance d and the output y readings. The dead-time is computed via cross-correlation of the post-processed signals. We note that during the control experiments, the time-delay τ is re-calibrated using the real-time processed signal to account for the additional time-lag from the low-pass filter. Once aligned, the set of measurements are averaged within their ensemble of repetitions. Finally, the resulting signals are low-pass filtered with a cutoff frequency of 80 Hz. An example of the pre- and post-processed signals along with their power spectral densities are shown in Fig. 6. The transfer function models are fit to the data for every α, δ, and X-wire position using MATLAB's `tfest` command [35]. The resulting models are transfer function matrices with two components, as follows

$$G_{yd}(s) = \left[G_{yd1}(s)\ G_{yd2}(s)\right] e^{-s\tau}, \tag{6}$$

where $e^{-s\tau}$ accounts for the time delay τ between input and output readings. The input to the transfer function matrix in Eq. (6) is a vector containing the flow velocity disturbances measured by the X-wire $d = [d_1\ d_2]^T = [U - U_\infty\ V]^T$, and

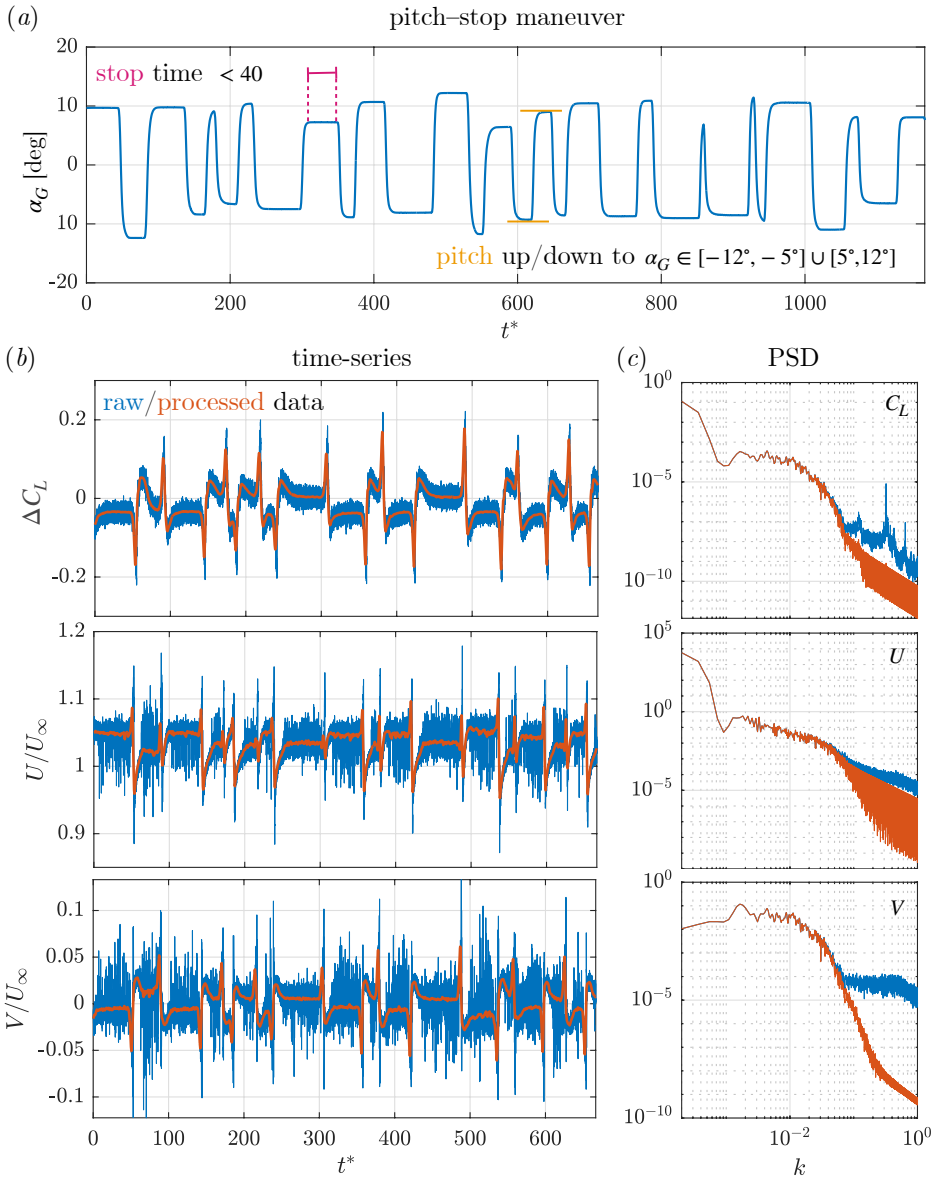

FIG. 6. (a) Gust generator angle of attack as a function of time during maneuver used to produce quasi-random gust encounters to identify the lift response model to gust disturbances. (b) Raw and processed signals of the unsteady lift coefficient $\Delta C_L = C_L - C_L^S$, and streamwise and vertical velocity components measured by the X-wire U and V, during quasi-random gust encounters. (c) Power spectral densities of raw and processed signals for ΔC_L, U, and V during quasi-random gust encounters.

the output is the unsteady lift coefficient $y = C_L - r$. The transfer function G_{yd} is a component of the feedforward controller G_{ff} expressed in Eq. (2). Different combinations of the number of poles and zeros are tested and the least complex models that accurately fit the data are transfer functions with two poles and two zeros, yielding transfer functions G_{yd1} and G_{yd2} of the same structure as G_{yu}. Because of this structure, the models have constant value asymptotes at low and high frequencies given by a_0/b_0 and a_2/b_2, respectively. The low-frequency asymptote corresponds to the *dc gain*, representing the increment in the static lift in response to an increment of the respective gust velocity components. The high-frequency gain represents the instantaneous increment in the unsteady lift when increasing the corresponding gust velocity component. However, attempting to provide a physical interpretation of the frequency asymptotes identified by our models may be misleading, since the gust disturbances of interest do not necessarily excite the full spectrum. Tables II and III show the identified coefficients for the transfer functions G_{yd1} and G_{yd2} for $\delta = 0°$ and $\alpha = 0°,\ 5°$ and $8°$.

To examine the models' robustness and identify their range of applicability, we compare the prediction error of

TABLE II. Identified coefficients for the first component of the transfer function for the lift response to disturbances G_{yd1} at various airfoil angles of attack α.

α	a_0	a_1	a_2	b_0	b_1	b_2
0 deg	-0.00155	0.00778	-0.00864	0.129	1.435	1.000
5 deg	0.00303	-0.00117	-0.00030	0.187	0.647	1.000
8 deg	0.00051	0.33160	0.00395	0.082	84.250	1.000

TABLE III. Identified coefficients for the second component of the transfer function for the lift response to disturbances G_{yd2} at various airfoil angles of attack α.

α	a_0	a_1	a_2	b_0	b_1	b_2
0 deg	0.00178	0.01557	0.05343	0.030	0.236	1.000
5 deg	0.02644	0.07991	0.04686	0.281	1.531	1.000
8 deg	0.00000	0.00533	0.04726	0.000	0.058	1.000

models trained at one nominal flap angle and tested at different angles. The normalized mean square error between the lift coefficient fluctuations predicted by the models and the data are shown in Fig. 7 (a) for several α and δ combinations. Comparison between the unsteady lift coefficient time-series at $\delta = 0°$ and $\alpha = 0°$, $5°$ and $8°$ are shown in Figs. 7 (b), (c), and (d), respectively. As Fig. 7 (a) shows for all airfoil angles, the models trained at $\delta = 0°$ extrapolate better to other flap deflection angles, as compared to models trained at $\delta = -5°$ and $5°$. We acknowledge the alternative approach to combine several linear models at different operating conditions into a parameter-varying model that is accurate over a larger envelope [30, 36].

Besides the data-driven models, we also assess Küssner's [7] model for the transient lift response of a thin airfoil entering a sharp-edged vertical gust, which was properly solved by von Kármán and Sears [8]. Using Duhamel's superposition integral, the theoretical lift response reads

$$C_L(t^*) = \frac{2\pi}{U_\infty}\left(V(0)\psi(t^*) + \int_0^{t^*} \frac{dV(\xi)}{\mathrm{d}t^*}\psi(t^* - \xi)\mathrm{d}\xi\right), \tag{7}$$

where ξ is an integration variable, and ψ is the Küssner function, which we compute using the approximation by Sears and Sparks [9]

$$\psi(t^*) \approx 1 - 0.5(e^{-0.13t^*} + e^{-t^*}). \tag{8}$$

For the numerical evaluation, the time derivative is approximated via finite-differences and then convolved with the Küssner function in Eq. (8) according to Eq. (7). The theoretical model performs surprisingly well, as shown by Figs. 7(b)-(d). The model accurately tracks the lift variations caused by arbitrary gust encounters, including both the primary and secondary lift peaks. The success of Küssner's model is unexpected because it relies only on the vertical velocity component V of the gust disturbance, whereas the vortical gusts studied include a streamwise component too, as shown in Fig. 8(a). This success is partially due to the much larger influence of V than U on the instantaneous flow response. This is confirmed using the identified model, which allows us to disambiguate the predicted contributions to the unsteady lift imparted by each gust velocity component. As shown in Fig. 8(b), the vertical velocity component V clearly contributes the most to the lift response. Note that, before and after the gust, the horizontal velocity component measured by the cross-wire does not exactly match the free-stream velocity U_∞ because of the gust generator wake. However, this does not play a significant role in the unsteady lift dynamics. We remark that the theoretical Küssner's model could be further improved when considering Greenberg's streamwise-varying gust model [10], which we intend to employ in future work.

Nonetheless, the theoretical model's accuracy remains lower than the empirical model given by Eq. (6). For this reason, and because it is easier to incorporate into the control loop, we choose the data-driven model Eq. (6) to perform control.

IV. RESULTS AND DISCUSSION

A. Gust generator wake characterization

This section presents our efforts in identifying and quantifying extraneous disturbances *besides* vortex gusts. This is motivated by the desire to disambiguate gust disturbances from other sources. The main source of extraneous

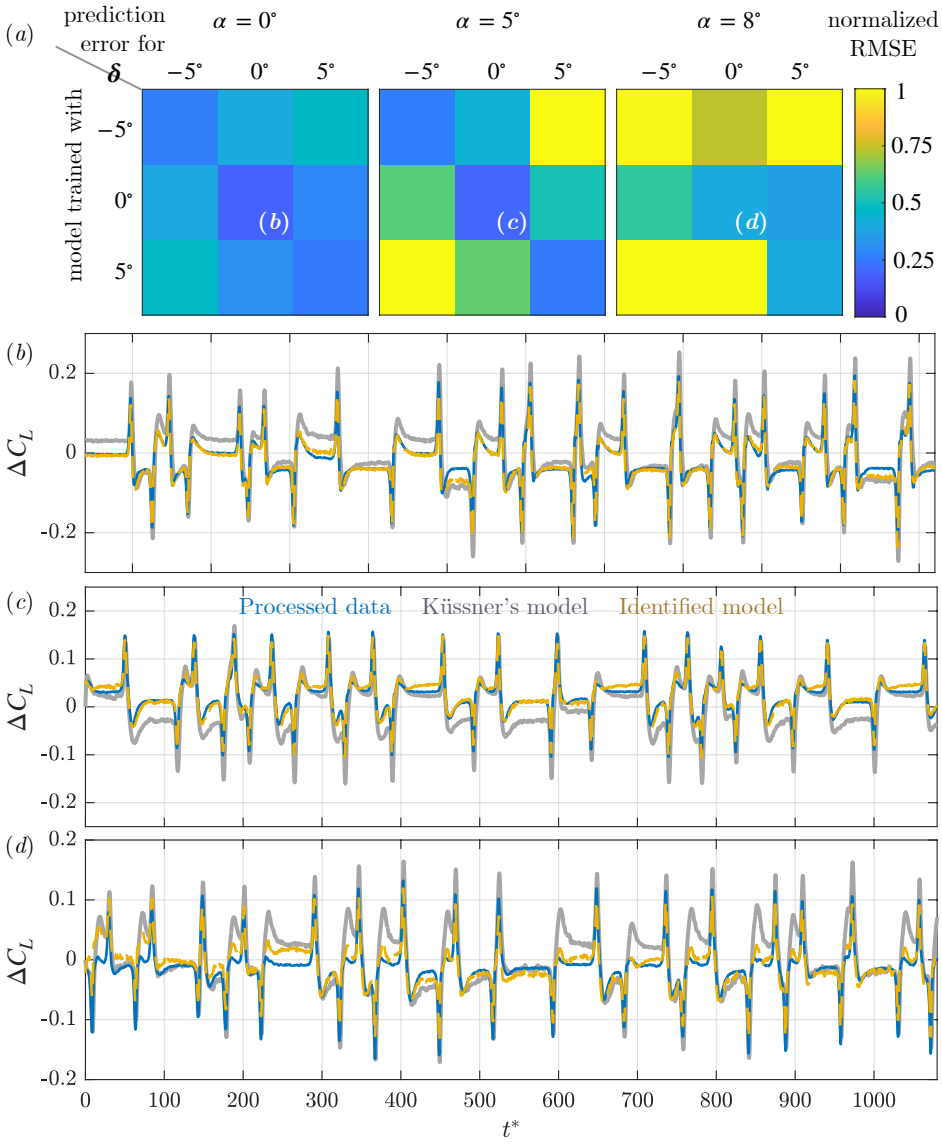

FIG. 7. (a) Prediction error on validation runs of models trained and tested at various α and δ combinations. Time-series of the unsteady lift coefficient $\Delta C_L = C_L - C_L^S$ from the processed validation data, predictions from the identified model, and predictions using Küssner's sharp-edged gust with Duhamel's superposition integral, at $\delta = 0°$ and (b) $\alpha = 0°$, (c) $\alpha = 5°$, and (d) $\alpha = 8°$. The white text labels inside (a) indicate the prediction errors that correspond to the time series shown in (b), (c) and (d).

disturbances stems from the steady gust generator airfoil wake, which is associated with increased incident velocity fluctuations. We characterize the wake effects and identify its path using a time-resolved pressure sensor at the research airfoil leading edge and the X-wire measurements upstream of the DLR-F15 airfoil.

The pressure coefficient standard deviation $\sigma(C_p^{\mathrm{LE}})$ at the airfoil leading edge is shown in Fig. 9 for the entire range of steady flap angles δ and gust airfoil angles of attack α_{G}. We emphasize that these tests are conducted under steady conditions for both the gust generator and the flap angle. As the figure shows, the gust generator wake affects the airfoil differently at different conditions. A wake impingement is identified with an elevated $\sigma(C_p^{\mathrm{LE}})$ above the undisturbed value of ≈ 0.016.

At $\alpha = 0\,°$, the research airfoil chordline aligns with the gust generator axis of rotation. Under these conditions, the gust generator wake impacts the DLR-F15 airfoil in an almost symmetrical pattern. The moderate asymmetry in the $\sigma(C_p^{\mathrm{LE}})$ distribution with respect to δ is caused by the asymmetric airfoil geometry that slightly displaces the wake path towards the airfoil suction side. With increasing δ, and thus with higher static circulation, the wake path (and streamlines) is gradually shifted upward until it bypasses the airfoil altogether. This is reflected in the flat part of

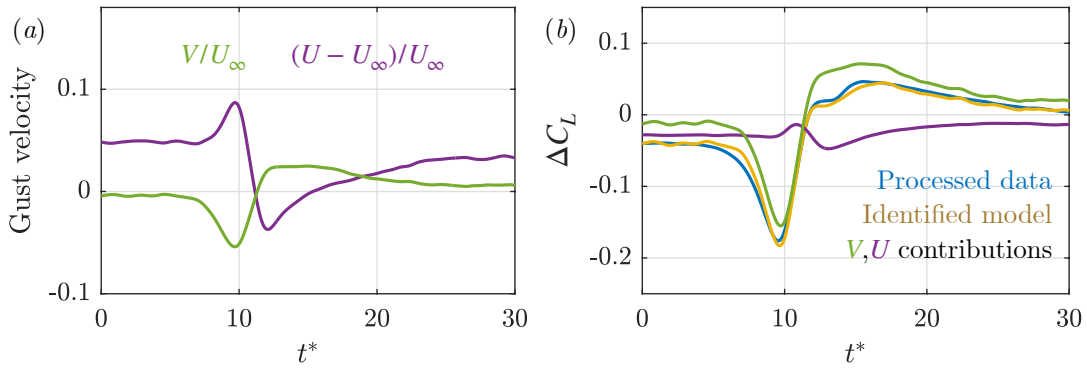

FIG. 8. (a) Processed streamwise and vertical velocity components measured by the X-wire during a gust encounter. (b) Unsteady lift coefficient during a gust encounter. Processed data is compared to model predictions considering only the vertical, only the streamwise, and both gust components. Case shown is for $\delta = 0°$ and $\alpha = 0°$.

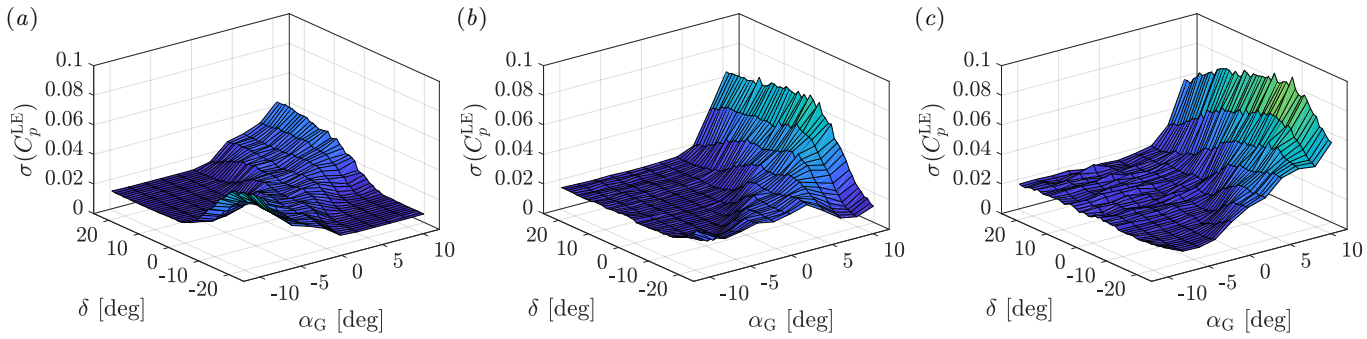

FIG. 9. Quantification of the gust generator wake on the research airfoil: Standard deviation distributions of the pressure coefficient C_p at the DLR-F15 leading edge for (a) $\alpha = 0\,°$, (b) $\alpha = 5\,°$, and (c) $\alpha = 8\,°$.

the distribution in Fig. 9(a), where the fluctuation level $\sigma(C_p^{\mathrm{LE}})$ reaches the undisturbed value. Similarly, decreasing flap angles shifts the wake path towards the airfoil pressure side.

The gust generator airfoil angle of attack α_{G} has an equally strong impact on the wake path. With increasing (decreasing) α_{G}, the streamlines are shifted downward (upward) until the gust generator wake path completely misses the DLR-F15 airfoil. In summary, the constant region on the left of the distribution in Fig. 9(a) is associated with conditions where the wake path is diverted above the airfoil, whereas the constant region to the right corresponds to wake diversion below the airfoil.

With increasing α, the research airfoil circulation increases, and as observed in Fig. 9(b) for $\alpha = 5\,°$, the wake path is further diverted towards the airfoil suction side. In fact, the entire distribution of Fig. 9(a) at $\alpha = 0\,°$ is translated to the right, indicating a shift in the range of wake path towards the suction side. Larger angle of attack maintain this trend with more streamline deviations in the upward direction, as observed in Fig. 9(c) for $\alpha = 8\,°$.

We emphasize that this wake path analysis is conducted at steady angles (α, δ, and α_{G}), where the wake effects are the strongest. Nonetheless, the gust generator wake impacts the airfoil minimally and the highest fluctuations ($\sigma(C_p^{\mathrm{LE}}) \approx 0.08$) remain tolerable. Smaller wake effects can be expected during gust generation when α_{G} is dynamically changing.

Another motivation to characterize the wake path concerns the positioning of the X-wire. Specifically, we seek a feedfoward sensor placement that best captures the incident disturbances on the research airfoil, while minimizing extraneous ones. Thus, we favor sensor positions with minimal streamline deflection and wake impingement. Using the X-wire measurements at the two explored locations, we compute the flow angle for the range of tested steady α_{G}. This angular change, denoted by $\varphi^{\mathrm{s}}_{\mathrm{XW}}$, quantifies the streamline deviation at the measured location. The $\varphi^{\mathrm{s}}_{\mathrm{XW}}$ distributions at the two X-wire positions are shown in Fig. 10. As can be seen, the effect is more pronounced at XW1, the position closer to the gust generator, where streamline deflections linearly change with α_{G} and reach $\varphi^{\mathrm{s}}_{\mathrm{XW}} \approx \pm 1.5\,°$ within the tested range. On the other hand, the streamline deflection at XW2, which is closer to the DLR-F15 airfoil, is significantly lower and remains within $\varphi^{\mathrm{s}}_{\mathrm{XW}} \approx \pm 0.5\,°$. As such, positioning the X-wire nearer to the research airfoil and further downstream from the deflected wake yields a more representative state of the incident conditions. As we

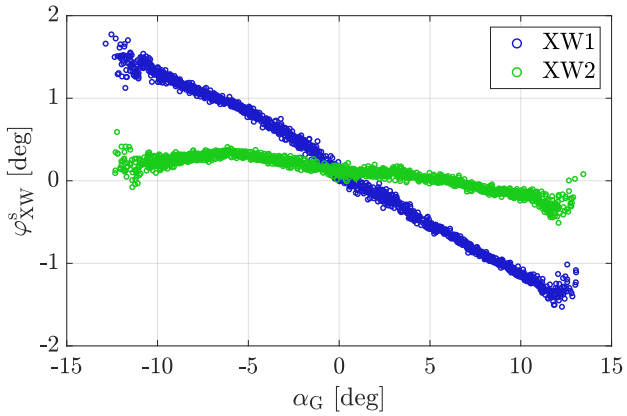

FIG. 10. Effect of static gust generator on the freestream flow angle φ^{s}_{XW} at the two X-wire positions for $\alpha = 0\,^\circ$.

detail in section IV C, this is also reflected in the controller performance in mitigating gusts.

B. Effect of gust encounters on the airfoil lift

Gust encounters are associated with variations in the effective angle of attack and thus the resultant forces and moments acting on the lifting body. In this section, we examine the impact vortical gusts have on the DLR-F15 airfoil lift coefficient *without* active mitigation efforts. Throughout this analysis, the flap position is kept constant at $\delta = 0\,^\circ$. The lift coefficient sequences for (a) periodic and (b) quasi-random gust encounters is shown in Fig. 11. As can be seen in Fig. 11(a) for a pitch-down motion of the gust generator, the convected periodic gusts incur periodic lift bursts in both directions. The first (primary) lift burst occurs shortly after the gust onset and yields a $\Delta C_L \approx \pm 0.18$ lift deviation $t^* = 2tU_\infty/c \approx 4$ after the *start* of the pitch down motion of the gust generator, which is mostly the time it takes for a gust to convect downstream and impinge on the airfoil. As the gust further convects downstream over the airfoil and nears the trailing edge, the airfoil experiences a lift change in the opposite direction. Experimental [14, 31] and numerical [37] analysis on sine-squared gust profiles have shown that this (secondary) lift change is caused by the formation of a large trailing edge vortex concentration of opposite-signed vorticity on the suction side of the airfoil. Such observations are also mirrored in Fig. 11(b) for a quasi-random motion sequence. The figure also shows how both the primary and secondary lift peaks scale with the gust amplitude, i.e., with the gust generator angular change $\Delta\alpha_G$, concurring previous results [14, 31, 37]. Surprisingly, multiple lift peaks with absolute lift coefficient values larger than those attained by periodic (or single) gusts for similar $\Delta\alpha_G$ are observed. These large lift bursts (e.g. lift burst near $t^* \approx 200$) can reach $\Delta C_L \approx 0.28$. They are caused by two concurrent gusts with opposite rotation near the leading and trailing edge acting synergetically on the airfoil to increase or decrease the lift. These observations extend to both clockwise–counterclockwise and counterclockwise–clockwise rotating gust combinations. Again, the slight asymmetry in the lift response is caused by the asymmetry of the DLR-F15 geometry. Such extreme lift bursts further demonstrate the possible dangers caused by lift encounters, particularly gust trains with alternating rotation.

The previous observations are also reflected in the probability density functions (P) of $\Delta C_L = C_L - C_L^s$ for the two gust motions and the three angles of attack presented in Fig. 12. For the periodic gusts in Fig. 12(a), the primary and secondary lift bursts are clearly visible, particularly at $\alpha = 0\,^\circ$. The slight asymmetric response is also well illustrated. Increasing the airfoil angle of attack has a clear influence on the lift response to gusts. Most notable is the reduction of the secondary positive lift peak in frequency and intensity. This suggests that the encountered clockwise-rotating gusts convect farther away from the airfoil trailing edge with increasing α, decreasingly impacting the airfoil loads. In contrast, the secondary negative lift peak is less affected, which indicates that counter-clockwise gusts remain close to the airfoil pressure side as they convect downstream. Detailed field measurements are required to confirm these findings.

In contrast to the periodic gust, the probability density functions of the lift response to quasi-random gusts are more broadly and randomly distributed (c.f. Fig. 12(b)). The broader distribution is the result of previously-mentioned synergetic gusts with opposite rotation simultaneously acting on the airfoil. Increasing α appears to mainly affect the positive tail of the distribution, decreasing the range by $\Delta C_L \approx 0.1$ between $\alpha = 0\,^\circ$ and $\alpha = 5\,^\circ$. The reason behind this observation is not entirely clear. We suspect this is caused by the stronger gust generator wake interaction with the DLR-F15 airfoil at $\alpha = 0\,^\circ$.

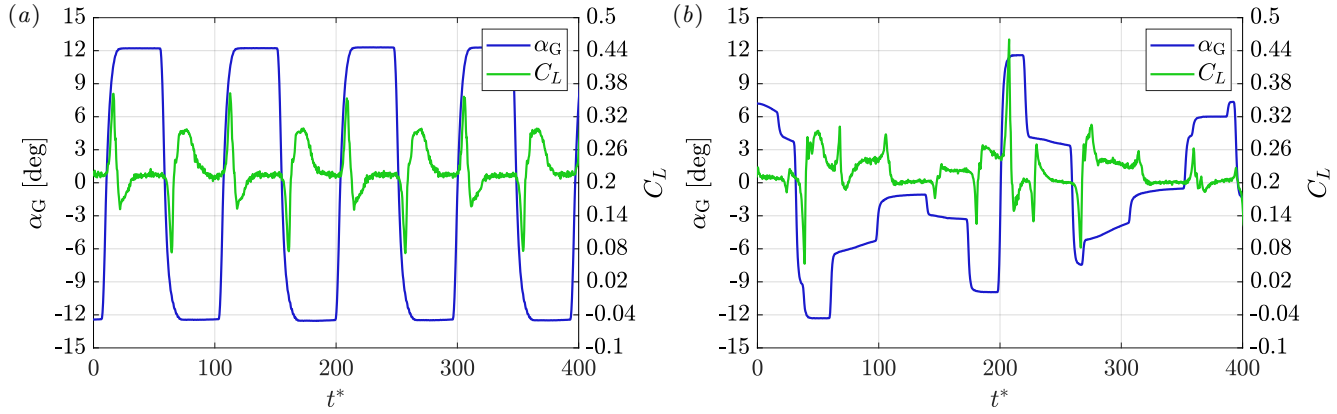

FIG. 11. The lift response to (a) periodic and (b) quasi-random gust patterns at $\alpha = 0\,^\circ$. Also shown is the corresponding gust generator angular sequence.

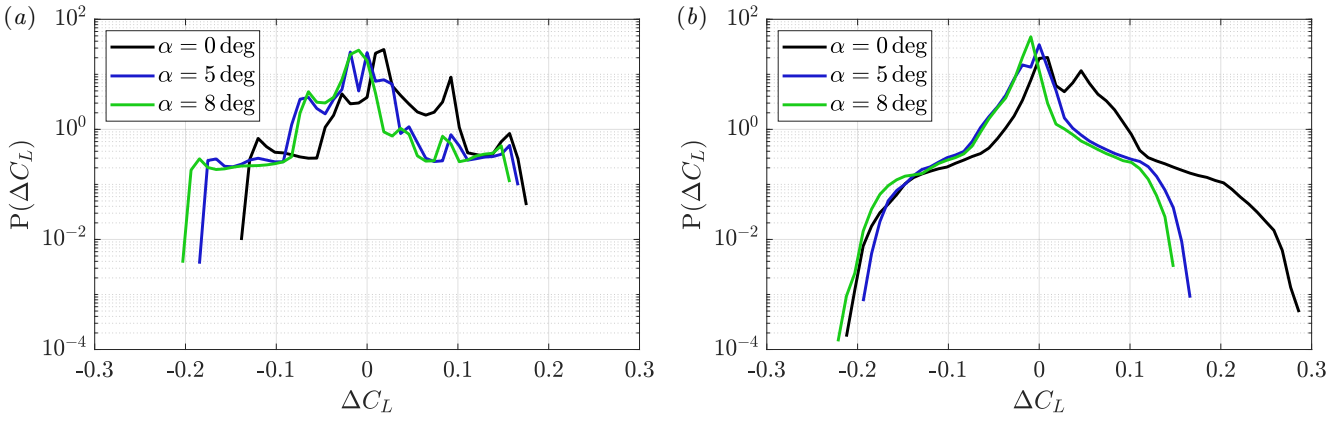

FIG. 12. The probability density functions of ΔC_L at $\alpha = 0, 5, 8\,^\circ$ for (a) periodic and (b) quasi-random gusts.

TABLE IV. List of the five tested control strategies and their acronyms.

Control strategy	Acronym	Feedback design	Feedforward design
Model-based feedback	MFB	model-based	–
PI-based feedback	PFB	PI	–
Model-based feedforward	MFF	–	model-based
Model-based feedback/model-based feedforward	MFB/MFF	model-based	Model-based
PI-based feedback/model-based feedforward	PFB/MFF	PI	model-based

C. Controller performance

The control architecture detailed in section III offers ample opportunities to examine various control strategies. A list of the five tested control strategies and their acronyms is provided in Tab. IV. We first compare the performance of control strategies with only feedback, both with the model-based MFB and the proportional-integral PFB controllers, to those with only feedforward MFF, and those with combined feedback and feedforward MFB/MFF and PFB/MFF. We assess the performance by examining the probability density function distributions of the controlled lift fluctuations y at $\alpha = 0°$ and $\delta_r = 0°$ during periodic and quasi-random gust encounters, as shown in Figs. 13(a) and (b), respectively. Here, δ_r denotes the reference flap angle at a corresponding target lift coefficient.

For both the periodic and the quasi-random gust encounters, the best performance in terms of gust load alleviation is observed for the PFB/MFF controller design. Here, we report a 58.6 % and 63.9 % reduction in the lift standard deviation for the periodic and quasi-random cases, respectively, compared to the uncontrolled case. The purely model-based MFB/MFF design shows a slightly degraded performance while employing the same feedforward model. This suggests a worse performance of the model-based feedback loop, compared to the PI feedback, which is also confirmed in a direct comparison of the respective feedback-only distributions, i.e., MFB versus PFB. We believe the PI-based

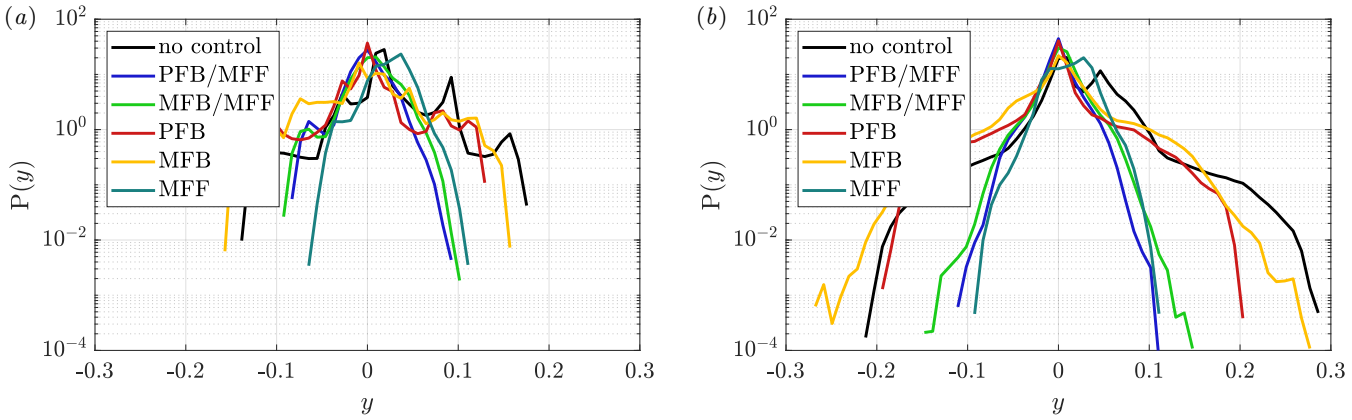

FIG. 13. Probability density functions of the lift fluctuations y for $\alpha = 0°$ and $\delta_r = 0°$ during (a) periodic and (b) quasi-random gust encounters using various control architectures: only feedback, both with the model-based MFB and the proportional-integral PFB controllers, only feedforward MFF, and combined feedback and feedforward MFB/MFF and PFB/MFF.

TABLE V. Performance summary of the five controller strategies applied on quasi-random gusts at $\delta_r = 0\,°$; y_{rms} quantifies the disturbance rejection, whereas $|\overline{y-r}|$ the reference tracking capabilities.

Control strategy	η	$\lvert\overline{y-r}\rvert$
MFB	−1.0	0.002
PFB	18.8	0.000
MFF	44.2	0.014
MFB/MFF	56.5	0.004
PFB/MFF	63.9	0.000

controller superiority is a consequence of both the simple linear model inversion used in the model-based feedback loop and the in-situ hand-tuning of the PI feedback controller. This superiority of PFB/MFF over the MFB/MFF extends to other angles of attack. Without any feedforward, the model-based feedback is not able to effectively mitigate the large amplitude lift fluctuations. This is because the feedback controller is designed for slow reference tracking rather than fast disturbance rejection. Nonetheless, both feedback controllers are capable of correcting for low-frequency deviations from the reference lift r, leading to centering of the respective distributions around $y = 0$. In contrast, feedforward control alone shows significant improvements in gust load alleviation. However, it is not able to center the probability density function distributions, leading to deviations from the reference lift. These observations are reflected in Tab. V for the five controllers, where

$$\eta = 100 \cdot \frac{y_{rms} - (\Delta C_L^{\text{uncontrolled}})_{rms}}{(\Delta C_L^{\text{uncontrolled}})_{rms}}\,, \tag{9}$$

is the percent y_{rms} reduction with respect to the uncontrolled case, and $|\overline{y-r}|$ is the mean deviation from the control setpoint. Whereas η quantifies the disturbance rejection capabilities, $|\overline{y-r}|$ characterizes the reference tracking.

To highlight the drastic lift fluctuation mitigation achieved with the combined feedback and feedforward PFB/MFF control compared to the cases without control (e.g., Fig. 11), we present in Fig. 14 lift time series for controlled cases at $\alpha = 0°$ and $\delta_r = 0°$. For both periodic and quasi-random gust disturbances, the use of control eliminates the characteristic primary and secondary lift peaks observed in the uncontrolled test cases. Small lift fluctuation peaks are still visible, however with a significantly reduced amplitude. In addition, the feedback loop stabilizes C_L around the tracked reference r. The corresponding flap deflection control signals are also shown in Fig. 14. As expected, sharp changes in the flap deflection mitigating the primary lift fluctuation succeeded by smaller angular deflections in the opposite direction to counter the secondary lift disturbance are observed at every gust encounter. The absolute flap deflection amplitude remains below 6 ° throughout all gust mitigation experiments.

During a gust encounter, the primary (maximum) and secondary (minimum) lift burst magnitude depends on the gust intensity and thus on $\Delta\alpha_G$. We quantify and visualize the burst amplitude of these extrema in Fig. 15 for each of the generated quasi-random gusts with and without control. For the uncontrolled case shown in Fig. 15(a), the distribution shows that the primary peak is stronger for positive $\Delta\alpha_G$, whereas the secondary peak is weaker compared to negative $\Delta\alpha_G$. This asymmetry is due to both the asymmetric airfoil geometry and to the occasional synergetic vortices. With control turned on, both the primary and secondary peaks are significantly mitigated, as

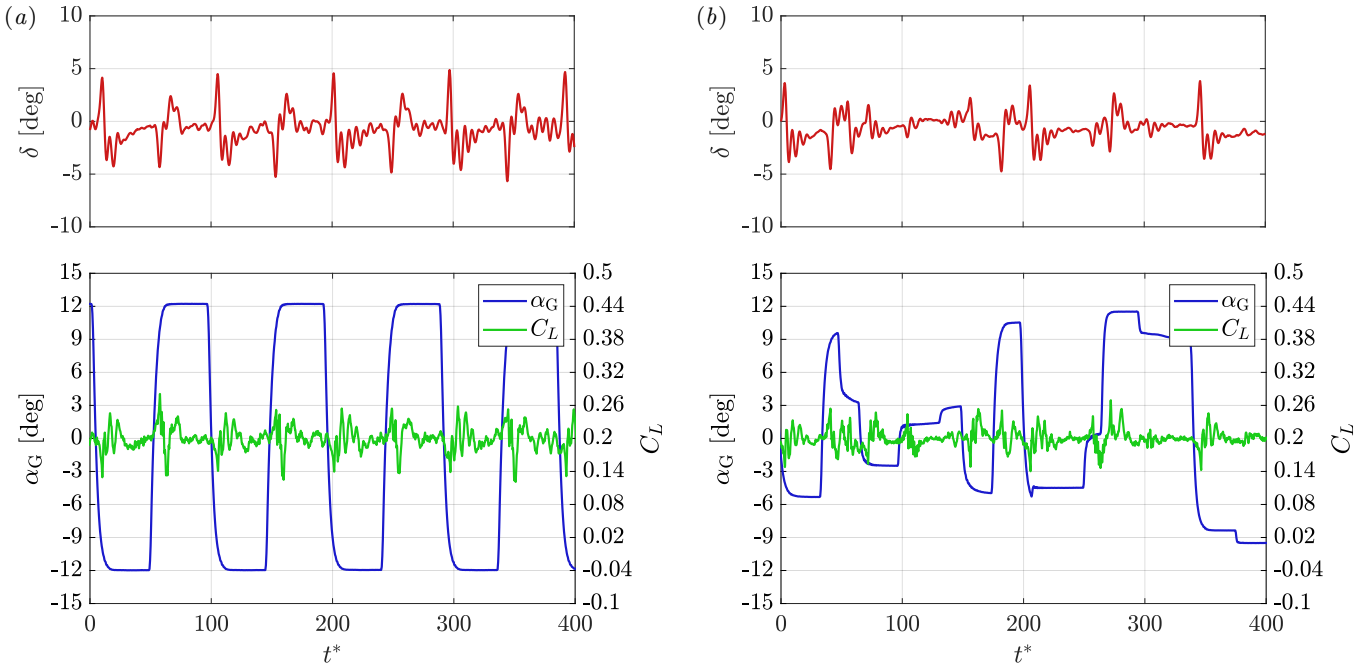

FIG. 14. Time series of the flap schedule, the lift coefficient and the gust generator angle of attack under closed-loop PFB/MFF control during (a) periodic and (b) quasi-random gust encounters with $\alpha = 0°$ and $\delta_r = 0°$.

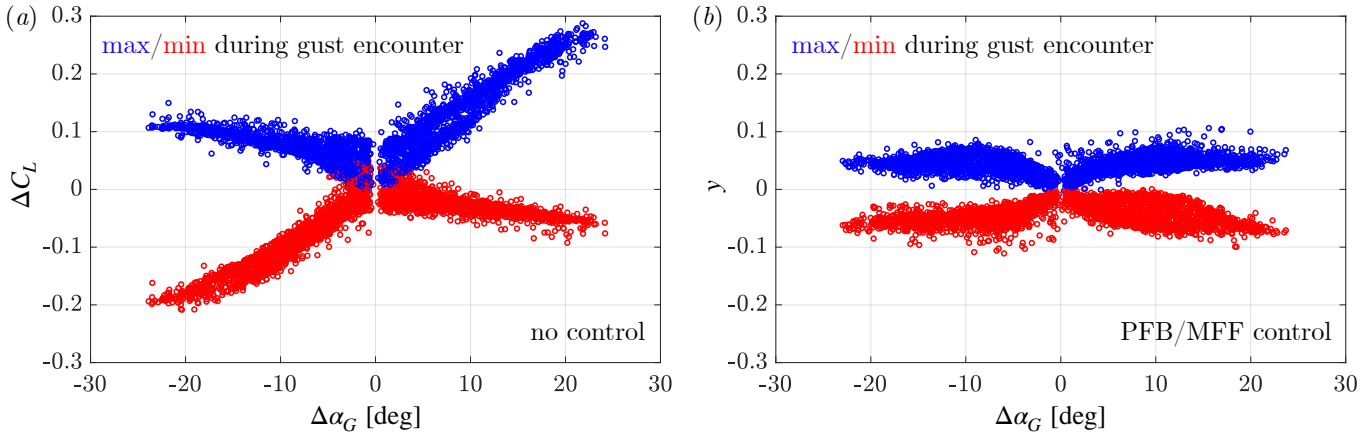

FIG. 15. Primary (maximum) and secondary (minimum) lift fluctuation magnitude captured for individual quasi-random gusts as a function of the corresponding gust generator amplitude $\Delta\alpha_G$ (a) without and (b) with feedback and feedforward PFB/MFF control at $\alpha = 0°$ and $\delta_r = 0°$. Lift fluctuations are reported as deviations from the static lift $\Delta C_L = C_L - C_L^s$ in (a) and as deviation from the control setpoint $y = C_L - r$ in (b).

shown in Fig. 15(b). The success of the control approach is clearly visible. Fluctuations in the airfoil lift are reduced below $|y| \leq 0.12$. Moreover, control renders the lift response symmetric around the origin, with both primary and secondary lift peaks reduced for every gust encounter.

Using the best performing control strategy, i.e., PFB/MFF, the probability density functions of the lift fluctuations at various α and δ_r combinations during quasi-random gust encounters are compared in Fig. 16. As Fig. 16(a) shows, the controller performance is similarly successful at the three airfoil angles of attack α. On the other hand, the reference flap deflection angle δ_r appears to affect the controller performance. A slightly worse performance is observed for $\delta_r = 5°$, evidenced by the larger variance of the lift fluctuations y in Fig. 16(b). This is not entirely surprising, as aggressive control maneuvers may cause flow separation and reduce the flap effectiveness at higher flap angles.

Thus far, we have only presented the controllers operating at on-design conditions. By this we mean that the

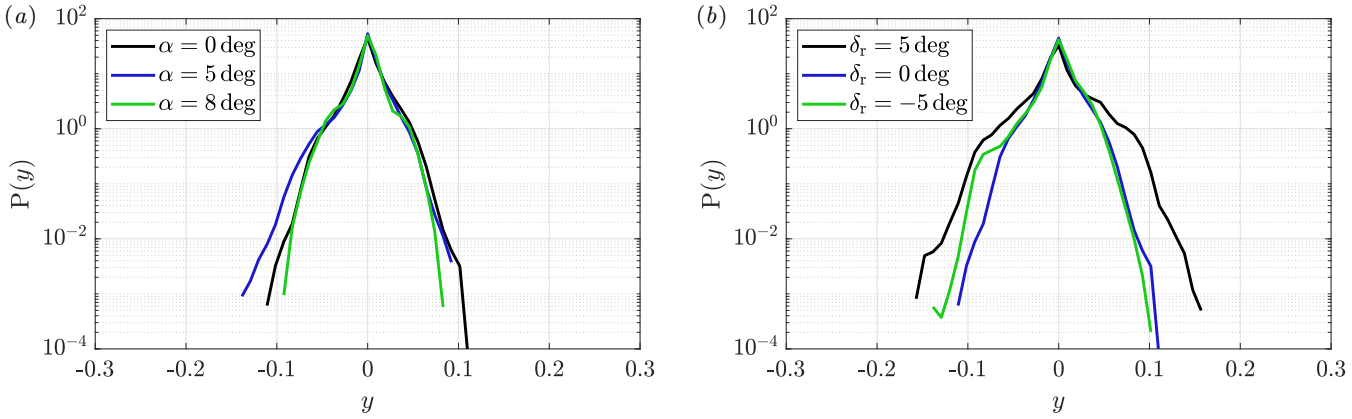

FIG. 16. Probability density functions of the lift fluctuations y during quasi-random gust encounters using PFB/MFF control for (a) $\alpha = 0°,\ 5°$, and $8°$ with $\delta_r = 0°$, and (b) for $\delta_r = -5°,\ 0°$, and $5°$ with $\alpha = 0°$.

TABLE VI. On- and off-design PFB/MFF controller performance at $\alpha = 0°$ during quasi-random gust encounters. The controller is based on input and disturbance response models trained at $\delta = 0\,°$ and tested to track a reference lift corresponding to $\delta_r = -5\,°$, $0\,°$, and $5\,°$.

Trained at δ [deg]	Tested at δ_r [deg]	η
0	−5	60.3
0	0	63.9
0	5	54.8

controllers are based on models G_{yu} and G_{yd} that are trained at a certain δ that is equal or close to the reference angle δ_r used for control. For off-design conditions, we assess a controller based on models trained at $\delta = 0\,°$ and tested at $\delta = -5\,°$, $0\,°$, and $5\,°$. As listed in Tab. VI, our control framework is capable of drastically reducing lift fluctuations during gust encounters, even using controllers based on models that are trained at a different flap deflection angle. This demonstrates the robustness of the employed model-based controllers beyond the training range.

V. CONCLUSIONS

In this work, we perform gust mitigation using closed-loop control with an active trailing edge flap in wind tunnel experiments at $Re = 1.8 \cdot 10^6$. The current undertaking is enabled by a dedicated experimental setup and a feedforward-feedback control strategy. Vortical gusts are generated upstream by a rapidly pitching NACA-0021 airfoil. The investigated airfoil is a DLR-F15 research airfoil, equipped with a $0.1\,c$ trailing-edge flap that is driven by two high-speed servomotors. The control strategy combines feedback control that is based on lift coefficient measurements and feedforward control that relies on two-component flow velocity readings from an X-wire sensor located upstream of the airfoil. The strategy builds on extensive analysis and modeling effort of the lift response to flap deflection and gust disturbances. In Part I of this series, the unsteady lift response to dynamic flap actuation is thoroughly investigated and modeled. Linear models are constructed from measurement data, relating the unsteady airfoil lift C_L to the flap deflection angle δ. In this second part of the series, we characterize and model the gust effects on the research airfoil, and employ them for control. Critical to the gust mitigation is the detection of the gust onset and its amplitude before impact, which we measure by an X-wire sensor positioned at two separate locations upstream of the test airfoil. The sensor location closest to the airfoil is deemed more suitable for control, exhibiting less interference from the gust generator wake. Importantly, our experimental setup remained fast enough to react despite the small time lead ($t \approx 13.9$ ms) that corresponds to the gust travel time between the sensor and the airfoil. The short reaction time is owed to the fully integrated FPGA programming and the powerful servo motors driving the flap.

The lift response to quasi-random gust encounters is measured at various airfoil angles of attack α and flap deflection angles δ. Synergetic behavior between two concurrent gusts with opposite rotation is observed to yield large lift bursts with a larger magnitude than that achieved by individual gusts with similar intensity. A family of linear models for the lift response to gust disturbances is identified from the measurements relating the measured velocity components U

and V to C_L. The models exhibit an accurate predictive performance on a validation dataset, with the models trained $\delta = 0°$ accurately extrapolating to other flap deflection angles. The models are also compared to Küssner's, which is originally developed for transverse gusts, showing a surprisingly good agreement that has not been reported at this Re. The success of Küssner's model is also unanticipated because it relies only on the vertical velocity component of the gust disturbance, whereas the vortical gusts studied include a streamwise component as well. We suspect this is due to the much larger influence of V on the instantaneous flow angle than U. With the incorporation of U as an input, our data-driven models notably outperform Küssner's model in their predictive capability.

Different closed-loop control strategies are compared, including model-based feedback, hand-tuned proportional-integral (PI) feedback, only feedforward, and combined feedback and feedforward controllers. The experimental results demonstrate the effectiveness of the combined approach in mitigating the lift fluctuations during quasi-random gust encounters at various α and δ. Compared to the uncontrolled case, we observe a 63.9 % reduction in the lift standard deviation during quasi-random gust encounters. While feedback control alone is insufficient to mitigate the gust effects in any meaningful manner, feedforward control relying on the identified models is very effective at reducing lift fluctuations. The role of feedback control is therefore to complement the fast disturbance rejection delivered by the feedforward by providing reference tracking while remaining robust to sensor noise. In this regard, both model-based (MFB/MFF) and model-free (PFB/MFF) feedback approaches showed similar results, with the hand-tuned PI performing slightly better.

The current methodology may guide future gust-mitigation studies using closed-loop control. One possible direction includes the use of a linear parameter-varying (LPV) control strategy, where several linear models are identified at different operating conditions and then used to create a set of controllers that may be combined, through interpolation or scheduling, to yield a more accurate and robust control over a larger envelope [30, 36]. This LPV modeling and control approach has been used recently in unsteady aerodynamic applications, where aggressive, large-amplitude maneuvers of a rigid airfoil are designed based on LPV models of the lift, drag, and pitching moment [38].

ACKNOWLEDGMENTS

The authors gratefully acknowledge the funding of the state of Lower-Saxony and the Technische Universität Braunschweig. SLB acknowledges funding support from the Army Research Office (ARO W911NF-19-1-0045).

[1] N. H. Al-Battal, D. J. Cleaver, and I. Gursul, Lift reduction by counter flowing wall jets, Aerospace Science and Technology **78**, 682 (2018).
[2] D. R. Williams and R. King, Alleviating unsteady aerodynamic loads with closed-loop flow control, AIAA Journal **56**, 2194 (2018).
[3] G. He, J. Deparday, L. Siegel, A. Henning, and K. Mulleners, Stall delay and leading-edge suction for a pitching airfoil with trailing-edge flap, AIAA Journal **58**, 5146 (2020).
[4] A. R. Jones, Gust encounters of rigid wings: Taming the parameter space, Physical Review Fluids **5**, 110513 (2020).
[5] H. Wagner, Dynamischer auftrieb von tragflugeln, Zeitschrift für angewandte Mathematik und Mechanik (1925).
[6] T. Theodorsen, *General Theory of Aerodynamic Instability and the Mechanism of Flutter*, NACA Report No. 496 (1935).
[7] H. G. Küssner, Zusammenfassender bericht über den instationären auftrieb von flügeln, Luftfahrtforschung **13**, 410 (1936).
[8] T. H. von Karman and W. R. Sears, Airfoil theory for non-uniform motion, Journal of the Aeronautical Sciences **5**, 379 (1938).
[9] W. R. Sears, Some aspects of non-stationary airfoil theory and its practical application, Journal of the Aeronautical Sciences **8**, 104 (1941).
[10] J. M. Greenberg, *Airfoil in sinusoidal motion in a pulsating stream*, Tech. Rep. (1947).
[11] J. G. Leishman, *Principles of Helicopter Aerodynamics*, 2nd ed. (Cambridge University Press, 2006).
[12] K. Granlund, B. Monnier, M. Ol, and D. Williams, Airfoil longitudinal gust response in separated vs. attached flows, Physics of Fluids **26**, 027103 (2014).
[13] R. Mark Rennie, B. Catron, M. Zubair Feroz, D. Williams, and X. He, Dynamic behavior and gust simulation in an unsteady flow wind tunnel, AIAA Journal **57**, 1423 (2019).
[14] G. Perrotta and A. R. Jones, Unsteady forcing on a flat-plate wing in large transverse gusts, Experiments in Fluids **58**, 1 (2017).
[15] H. Biler, C. Badrya, and A. R. Jones, Experimental and computational investigation of transverse gust encounters, AIAA Journal **57**, 4608 (2019).
[16] X. He, K. J. Asztalos, J. Henry, S. T. M. Dawson, and D. R. Williams, Generating traveling cross-flow gusts in a wind tunnel, in *AIAA Scitech 2021 Forum* (2021) p. 1938.
[17] S. Corkery, H. Babinsky, and J. Harvey, On the development and early observations from a towing tank-based transverse wing–gust encounter test rig, Experiments in Fluids **59**, 1 (2018).

[18] S. Klein, D. Hoppmann, P. Scholz, and R. Radespiel, High-lift airfoil interacting with a vortical disturbance: wind-tunnel measurements, AIAA Journal **53**, 1681 (2015).
[19] E. A. Hufstedler and B. J. McKeon, Vortical gusts: experimental generation and interaction with wing, AIAA Journal **57**, 921 (2019).
[20] J. Pohl and R. Semaan, Quantification and modeling of dynamic lift on a DLR-F15 research airfoil with active trailing-edge flap, in *AIAA Scitech 2020 Forum* (American Institute of Aeronautics and Astronautics, Orlando, FL, 2020).
[21] T. Colonius, C. W. Rowley, G. Tadmor, D. Williams, K. Taira, W. Dickson, M. Gharib, and M. Dickinson, Closed-loop control of leading-edge and tip vortices for small uav, in *Conference on Active Flow Control, DFG, Berlin*, Vol. 2729 (2006).
[22] K. Taira, W. Dickson, T. Colonius, M. Dickinson, and C. Rowley, Unsteadiness in flow over a flat plate at angle-of-attack at low Reynolds numbers, in *45th AIAA Aerospace Sciences Meeting and Exhibit* (2007) p. 710.
[23] J. D. Eldredge and A. R. Jones, Leading-edge vortices: mechanics and modeling, Annual Review of Fluid Mechanics **51**, 75 (2019).
[24] J. D. Eldredge, *Mathematical modeling of unsteady inviscid flows* (Springer, 2019).
[25] D. Darakananda and J. D. Eldredge, A versatile taxonomy of low-dimensional vortex models for unsteady aerodynamics, Journal of Fluid Mechanics **858**, 917 (2019).
[26] W. Kerstens, J. Pfeiffer, D. Williams, R. King, and T. Colonius, Closed-loop control of lift for longitudinal gust suppression at low Reynolds numbers, AIAA journal **49**, 1721 (2011).
[27] S. L. Brunton, C. W. Rowley, and D. R. Williams, Reduced-order unsteady aerodynamic models at low Reynolds numbers, Journal of Fluid Mechanics **724**, 203 (2013).
[28] S. L. Brunton and C. W. Rowley, Empirical state-space representations for Theodorsen's lift model, Journal of Fluids and Structures **38**, 174 (2013).
[29] S. L. Brunton, S. T. M. Dawson, and C. W. Rowley, State-space model identification and feedback control of unsteady aerodynamic forces, Journal of Fluids and Structures **50**, 253 (2014).
[30] M. S. Hemati, S. T. M. Dawson, and C. W. Rowley, Parameter-varying aerodynamics models for aggressive pitching-response prediction, AIAA Journal , 1 (2016).
[31] G. Sedky, A. R. Jones, and F. D. Lagor, Lift regulation during transverse gust encounters using a modified Goman–Khrabrov model, AIAA Journal **58**, 3788 (2020).
[32] J. Pohl, R. Semaan, and A. R. Jones, Dynamic lift measurements on an airfoil with periodic flap motion at high Reynolds number, in *AIAA Scitech 2019 Forum* (American Institute of Aeronautics and Astronautics, San Diego, California, 2019).
[33] S. Skogestad and I. Postlethwaite, *Multivariable feedback control: analysis and design*, Vol. 2 (New York: Wiley, 2007).
[34] R. Semaan and V. Yadav, Scout: signal correction and uncertainty quantification toolbox in matlab, SoftwareX **11**, 100474 (2020).
[35] A. A. Ozdemir and S. Gumussoy, Transfer function estimation in system identification toolbox via vector fitting, IFAC-PapersOnLine **50**, 6232 (2017).
[36] T. Shaqarin, P. Oswald, B. N. Noack, and R. Semaan, Drag reduction of a D-shaped bluff-body using linear parameter varying control, Accepted for publication in Physics of Fluids (2021).
[37] C. Badrya and J. D. Baeder, Numerical study of a flat plate wing response to large transverse gusts at low Reynolds number, in *AIAA Scitech 2019 Forum* (2019) p. 0638.
[38] N. Fonzi, S. L. Brunton, and U. Fasel, Data-driven nonlinear aeroelastic models of morphing wings for control, Proceedings of the Royal Society A **476**, 20200079 (2020).